Section 7

Global and regional climate models, sensitivity and impact experiments, response to external forcing, monthly and seasonal forecasting.

Improved representation of super-cooled liquid water cloud in JMA's next-generation coupled seasonal prediction system

CHIBA Jotaro* and KOMORI Takuya
Climate Prediction Division, Japan Meteorological Agency, Tokyo, Japan
(Email: jotaro-chiba@met.kishou.go.jp)

1 Introduction

The Japan Meteorological Agency (JMA) is developing the next-generational seasonal ensemble prediction system (JMA/MRI-CPS3; CPS3) for the purpose of supporting three-month, warm-/cold-season and El Niño forecasts. Some investigations have shown that a lack of supercooled liquid water (SLW) at the low-level cloud top causes radiation biases associated with underestimation of cloud amount and optical thickness (Kay et al., 2015) in CPS3. Accordingly, the authors tackled this issue via a pragmatic approach as an operational center to provide better forecasts. This report outlines the method and results.

2 Method

To represent the effects of SLW near the top of low-level cloud, the cloud ice ratio is calculated using an alternative diagnostic function of temperature that enables SLW presence down to a temperature of 238.15 (K)[1], and the deposition rate is reduced over the 500 (m) depth near the cloud top following the formulation of ECMWF (2018). The former change is also applied to the radiation scheme in calculating cloud optical thickness.

3 Results

The results of one-day experiments using the atmospheric component of CPS3 (TL319L100) with and without the modified cloud and radiation schemes were compared with the DARDAR-MASK product (Delanoë and Hogan, 2010), which contains vertical profiles of cloud phase extracted from the CALIPSO and CLOUDSAT satellite products. Along the satellite orbit on 8th Feb. 2010 (the red line in Figure 1), results from the TEST experiment with the modified schemes represent SLW near the cloud top from 160 to 165°E better than CNTL with the original schemes (Figure 2). Upward shortwave radiative flux at the top of the atmosphere is increased, and related error is smaller since lower-cloud cover and SLW increase (not shown).

Radiative biases were also evaluated through one-year experiments with observation data on sea surface temperature and sea ice concentration. Consistent with previous research, the most remarkable change is the wintertime improvement of shortwave radiation in the Southern Ocean, where low-level cloud with SLW near the top is commonly present (Figure 3). Overall, the revision of the schemes demonstrates significant improvement.

Reference

Delanoë, J., and R. J. Hogan, 2010: Combined CloudSat-CALIPSO-MODIS retrievals of the properties of ice clouds. J. Geophys. Res., 115, D00H29, doi:10.1029/2009JD012346.

European Centre for Medium-Range Weather Forecasts, 2018: IFS Documentation CY45R1, Part IV:Physical Processes, Chapter 7: Clouds and large-scale precipitation.

Kay, J. E., L. Bourdages, N. Miller, A. Morrison, V. Yettella, H. Chepfer, and Eaton, B., 2015: Evaluating and improving cloud phase in the Community Atmosphere Model version 5 using spaceborne lidar observations. J. Geophys. Res. Atmos., 121, 4162-4176.

[1] The current function cannot generate SLW at temperatures lower than 258.15 (K).

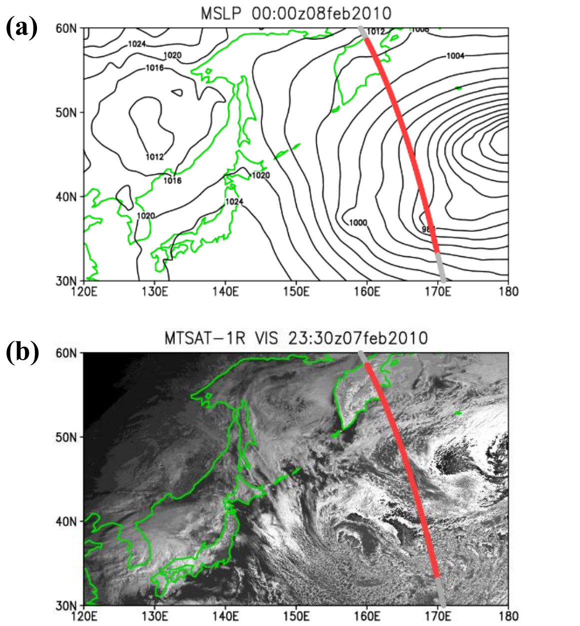

Figure 1 Satellite orbit in the DARDAR product (red line) and **(a)** Sea level pressure from JRA-55 reanalysis (contours) **(b)** Himawari-6 visible image

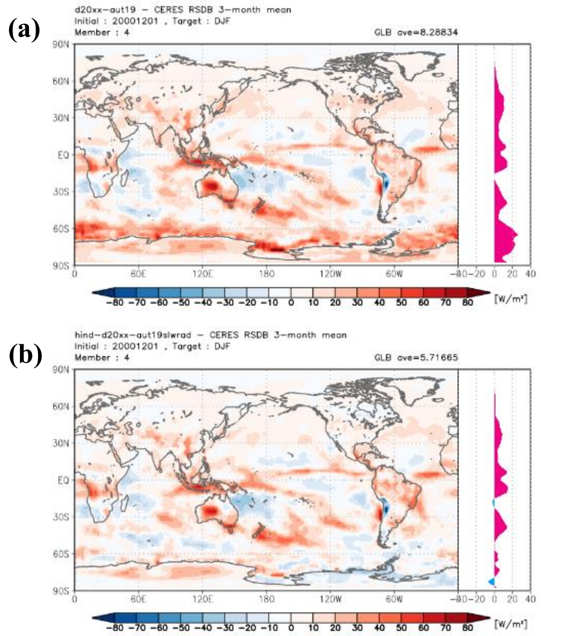

Figure 3 Bias of surface downward shortwave radiation flux against CERES-EBAF v2.8 in winter (DJF) from the **(a)** CNTL and **(b)** TEST experiments

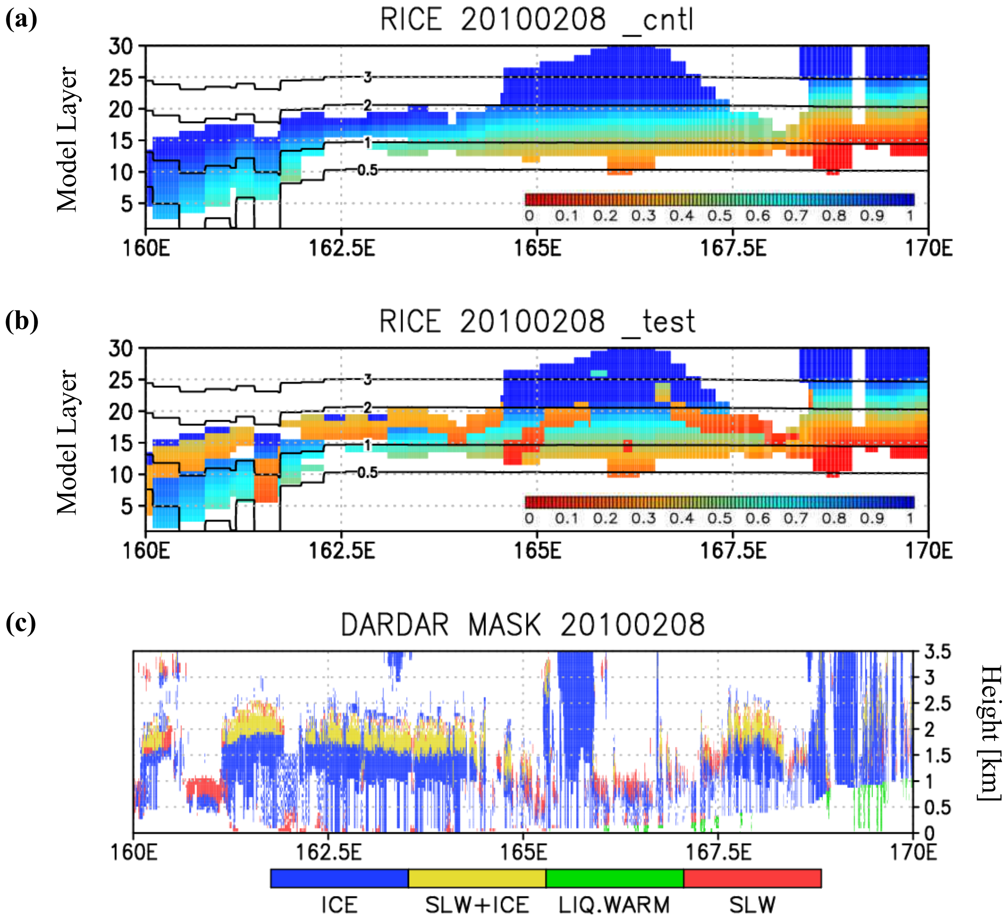

Figure 2 Cloud ice ratio (shading) and geopotential height [km] (contours) for the **(a)** CNTL and **(b)** TEST experiments. Cloud/precipitation phase categorization (shading) of the DARDAR-MASK product is shown in **(c)**.

Uncertainty of modeled wetland area and methane emissions from HBL due to climatic noise

S.N. Denisov, M.M. Arzhanov
A.M. Obukhov Institute of Atmospheric Physics, RAS
denisov@ifaran.ru

The ensemble of numerical experiments with a joint model of the methane cycle and heat and moisture transport in soil was performed forced by data from the atmospheric general circulation model ECHAM5 for Hudson Bay Lowlands (HBL) region.

The wetland methane emission model consists of two modules. In the methane emission module, the flux of methane from the soil to the atmosphere is calculated using the parameterization of the temperature dependence of methane production by bacteria. It also takes into account the dependence of emissions on the amount of the carbon substrate in the active soil layer [1, 2]. Necessary physical characteristics of the soil are calculated in the module of heat and moisture transport, which can reproduce the dynamics of the soil temperature fields in case of alternating several boundaries of thawed and frozen layers [3]. In past similar experiments, the constant wetland mask [4] was used. Now the model is supplemented with an interactive scheme for calculating the area of the model cell occupied by the wetlands based on TOPMODEL [5].

An ensemble of 45 realizations of the multi-year data of meteorological variables at the land surface, calculated by the ECHAM5 for different initial and identical boundary conditions for a 34-year period (from 1.01.1979 to 31.12.2012) was specified as space-distributed input data. The initial conditions (the state of the atmosphere for January 1, 1979) were specified as instantaneous atmospheric conditions at various 12-hour intervals in December 1978. Averages and standard deviations of annual and monthly wetland area and emission values were estimated, and in case of monthly indicators only months with significant (>0.1 $MtCH_4$) emission, i.e., May-October were selected. The 95% confidence intervals of these estimates were calculated as indicators of the variability of the obtained estimates of mean values and standard deviation due to the internal variability of the climate system. When calculating the confidence intervals, it was assumed that the corresponding estimates were subject to a Gaussian distribution of probability. The ratio of half of the width of the 95% confidence interval of the corresponding estimate to its average value was considered to be the indicators of uncertainty of the calculated estimations.

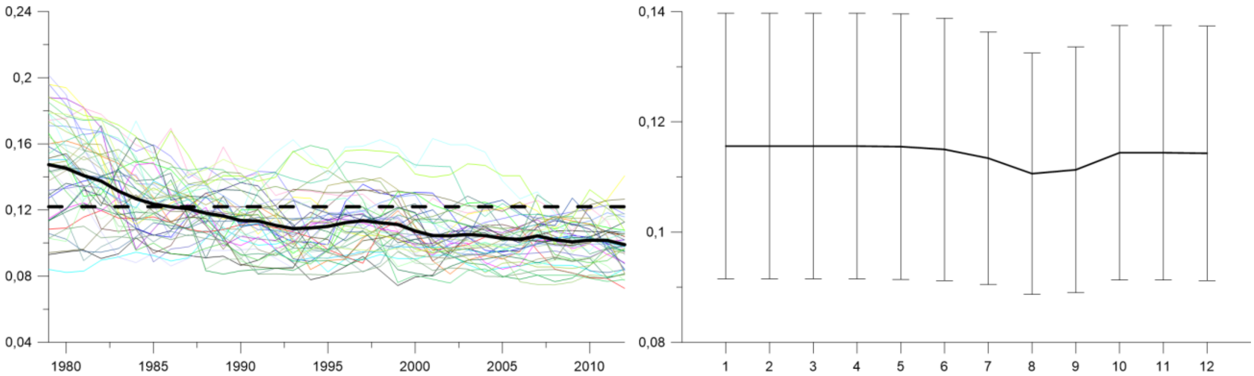

Fig.1 Simulated part of HBL region, covered by wetlands. Yearly means for each model realization (left) and monthly ensemble mean with standard deviation (right, month numbers on x axis). Thick line represents the ensemble mean, dashed line is the constant wetland mask data.

Wetlands are estimated to occupy 8-20% of HBL region area (Fig. 1). The ensemble average of yearly mean wetland area over the estimated period equals 11.4% (uncertainty index is 21%). The trend of wetland area equals -0.1%/yr. In some years, the wetland area may differ more than twice for different model realizations. On average, modeled wetland area tends to decrease slightly in the second half of summer and then recovers by the end of the year. For individual months, the uncertainty index of area remains within 21-22%.

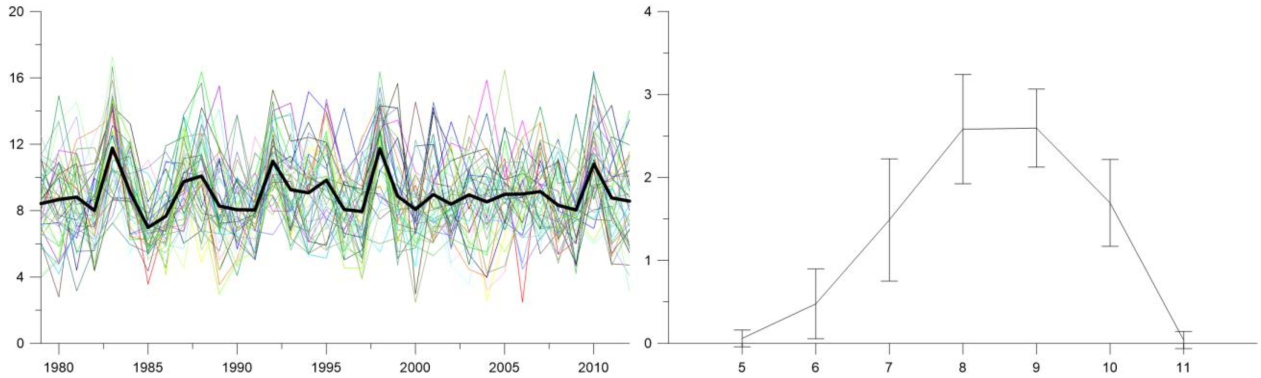

Fig.2 Modeled methane emissions [TgCH4/yr] from HBL wetlands on yearly and monthly scale (month numbers on x axis) in experiments with constant wetland mask.

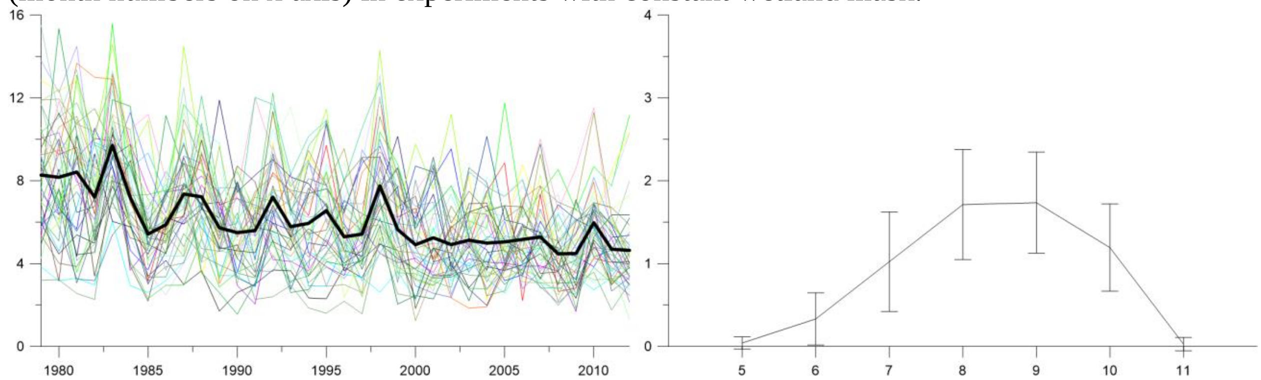

Fig.3 Modeled methane emissions [TgCH4/yr] from HBL wetlands on yearly and monthly scale (month numbers on x axis) in experiments with interactively calculated wetland area.

Estimations of methane emissions from HBL wetlands for 1979-2012 periods were obtained (Fig. 2,3) both with constant wetland mask and interactively calculated wetland area. With constant wetland mask the ensemble average of annual emissions over the estimated period equals 8.9 TgCH4 (uncertainty index is 11%). The trend of emissions is about 0.002 TgCH4/yr. The interactive calculation of the wetland area changes the emission parameters (especially the uncertainty) significantly. In this case the ensemble average of annual emissions over the estimated period equals 6.1 TgCH4 (uncertainty index is 32%). The trend of emissions is -0.1 TgCH4/yr. Total annual emissions in individual years may differ by more than 5 times between different realizations of the model. The highest methane flux estimations (more than 2 TgCH4) were obtained for August-September. For individual months, the uncertainty index of emission mean values equals 7-30% and 31-38% for constant and interactive wetlands correspondingly, and it is minimal for months with maximal emissions. The pronounced seasonal variability of uncertainty the emission values, inherent to calculations with constant wetland mask, mostly disappears in experiments with interactive wetlands.

This work is supported by Russian Foundation for Basic Research (18-05-00087, 18-05-60111 and 19-05-00409) and RAS.

References

[1] Eliseev A.V., Mokhov I.I., Arzhanov M.M., Demchenko P.F., Denisov S. N. Interaction of the methane cycle and processes in wetland ecosystems in a climate model of intermediate complexity // Izv. Atmos. Ocean. Phys. (2008) 44: 139.

[2] Denisov S. N., Eliseev A. V., Mokhov I. I., Arzhanov M.M. Model estimates of global and regional atmospheric methane emissions of wetland ecosystems // Izvestiya Atmospheric and Oceanic Physics V. 51. I. 5. P. 482-487. 2015.

[3] Arzhanov M.M., Eliseev A.V., Mokhov I.I. Impact of climate changes over the extratropical land on permafrost dynamics under RCP scenarios in the 21st century as simulated by the IAP RAS climate model // Russ. Meteorol. Hydrol. (2013) 38: 456.

[4] Bergamaschi P., Frankenberg C., Meirink J.F. et al. Satellite chartography of atmospheric methane from SCIAMACHY on board ENVISAT 2. Evaluation based on inverse model simulations // J. Geophys. Res.: Atm. 2007. V. 112. № D2. P. D02304.

[5] Beven, K. J. and Kirkby, M. J. A physically based variable contributing area model of catchment hydrology, Hydrol. Sci. Bull., 1979, 24, 43-69.

Long-Term High-Resolution North Atlantic Atmospheric Hindcast for Multipurpose Applications

Alexander Gavrikov*[1], Sergey K. Gulev[1,2], Margarita Markina[1,2], Natalia Tilinina[1], Polina Verezemskaya[1], Bernard Barnier[1,3], Ambroise Dufour[1,3], Olga Zolina[1,3], Yulia Zyulyaeva[1], Mikhail Krinitsky[1], Ivan Okhlopkov[2], Alexey Sokov[1]

1. Shirshov Institute of Oceanology, Russian Academy of Sciences, Moscow, Russia

2. Moscow State University, Moscow, Russia

3. Institut des Géosciences de l'Environnement, Grenoble, France

*Email: gavr@sail.msk.ru

Introduction

It is a well accepted expectation that increasing of model resolution will significantly improve the output quality due to the opportunity to explicitly resolve subsynoptic and mesoscale processes. There are evidences of the paramount impact of mesoscale dynamics in forming cold-air outbreaks (Kim et al. 2016, among others) and generating polar lows (Kolstad et al. 2016, among others); also mesoscale-resolving models provide more realistic clouds which in turn leads to more accurate radiation balance (Schneider et al. 2019, among others).

All of these phenomena cannot always be adequately captured by the coarse grid of global reanalyses. There is an urgent demand from different communities for long-term high-resolution atmospheric hindcasts performed with high-resolution model configurations for the North Atlantic where subsynoptic and mesoscale processes are of high relevance. Facing this challenge, the P.P. Shirshov Institute of Oceanology of the Russian Academy of Sciences (IORAS) in cooperation with the Institut des Géosciences de l'Environnement (IGE) developed a high-resolution (14 km) atmospheric downscaling experiment for the North Atlantic Ocean (North Atlantic Atmospheric Downscaling, NAAD).

Model description

In NAAD we used the nonhydrostatic WRF Model, version 3.8.1 (Skamarock et al. 2008). The domain (Fig. 1, A) covers the North Atlantic from 10 to 80N and from 90W to 5E, with the center at 45N, 45W. The initial and lateral boundary conditions (including sea surface temperature (SST)) were provided by the ERA-Interim reanalysis (Dee et al. 2011). The spatial resolution in the basic NAAD high-resolution experiment (HiRes) was 14km and 50 terrain-following, dry hydrostatic pressure levels, starting from around 10–12m above the ocean surface to 50 hPa with 15 levels in the boundary layer. Besides the HiRes experiment, we also conducted a moderately low resolution experiment (LoRes) with the hydrostatic setting of the WRF Model at 77-km resolution with 50 vertical levels (as in HiRes). The LoRes experiment (with resolution comparable to ERA-Interim) will be used to quantify the added value of the HiRes experiment, which cannot be directly compared with ERA-Interim (due to the fact that different models were used). All experiments were run for the 40-yr period from January 1979 to December 2018.

We conducted more than 32 sensitivity tests to determine the most suitable model configuration for the North Atlantic region. The configuration turned out to be very similar to the one used in Polar WRF of ARSv2 (Bromwich et al. 2018). Details of the model settings for the HiRes and LoRes experiments could be found in Gavrikov et al. (2020).

In order to constrain (nudge) the interior of both LoRes and HiRes experiments toward the larger-scale driving field, we applied throughout the 40-yr period the procedure of spectral interior nudging (Jeuken et al. 1996). Configuration of nudging was set according to the sensitivity study of Markina and Gavrikov (2016), which implied the optimal wavelength cut-off being 1100 km, applied only above the PBL. For determining the optimal nudging strength, we performed 18 sensitivity experiments with the nudging strength coefficients increasing from 3x10-5 to 3x10-3 s-1. These experiments implied an optimal value of the nudging strength coefficient of 3x10-4 s-1 (equivalent to a damping scale of about 1 h). This value is also consistent with other studies (Otte et al. 2012; Tang et al. 2017, among others).

Results

As an example, we provide the diagnosis of intense polar mesocyclone on March 2, 2008 near the southern tip of Greenland (Fig. 1). The wind field in NAAD HiRes (B) reveals polar low in more details comparing with ERA-Interim (C) atmospheric reanalysis. Notably HiRes results are very similar to ARSv2 (D) reanalysis due to similar models and resolution. NAAD HiRes detects well the location of the pressure minimum identifying a 978-hPa central pressure, which is deeper than that in ERA-Interim (986 hPa) and even in ERA5 (not shown). Also, NAAD HiRes demonstrates the well-detectable comma-type structure not present in ERA-Interim and ERA5 (not shown) and less evident in ASRv2.

The NAAD dataset includes prognostic and di-

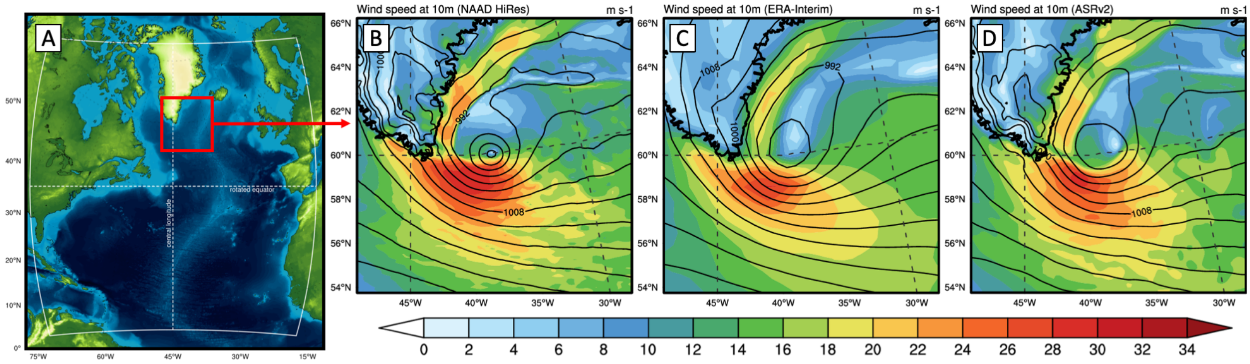

Figure 1: NAAD domain (A), diagnostics of the polar low on 2 Mar 2008. Shown is the surface 10-m wind speed (colors) and mean sea level pressure (MSLP; contours) as revealed by (B) NAAD HiRes, (C) ERA-Interim and (D) ASRv2.

agnostic variables at the surface and in the atmosphere at resolutions 14 km and 77 km for the period of 1979 to 2018. Coarse resolution was used to quantify the added value of the high-resolution experiment. All variables are provided at the native grids both for LoRes and HiRes experiment. The entire archive of the NAAD data amounts to 150 terrabytes (TB) with individual annual files ranging from approximately 140 MB in LoRes to 3.3 GB in HiRes for surface variables on to 165 GB for HiRes 3D fields. The whole NAAD data output is organized as annual NetCDF files by variable and is available online for download using Open-source Project for a Network Data Access Protocol (OPeNDAP) accesses at http://www.naad.ocean.ru.

References

Bromwich, D. H., and Coauthors, 2018: The arctic system reanalysis, version 2. *Bulletin of the American Meteorological Society*, **99 (4)**, 805–828, doi: 10.1175/BAMS-D-16-0215.1.

Dee, D. P., and Coauthors, 2011: The ERA-Interim reanalysis: configuration and performance of the data assimilation system. *Quarterly Journal of the Royal Meteorological Society*, **137 (656)**, 553–597, doi:10.1002/qj.828.

Gavrikov, A., and Coauthors, 2020: RAS-NAAD: 40-yr High-Resolution North Atlantic Atmospheric Hindcast for Multipurpose Applications (New Dataset for the Regional Mesoscale Studies in the Atmosphere and the Ocean). *Journal of Applied Meteorology and Climatology*, **59 (5)**, 793–817, doi:10.1175/JAMC-D-19-0190.1, URL `https://doi.org/10.1175/JAMC-D-19-0190.1`.

Jeuken, A. B., P. C. Siegmund, L. C. Heijboer, J. Feichter, and L. Bengtsson, 1996: On the potential of assimilating meteorological analyses in a global climate model for the purpose of model validation. *Journal of Geophysical Research Atmospheres*, **101 (D12)**, 16 939–16 950, doi:10.1029/96JD01218.

Kim, W. M., S. Yeager, P. Chang, and G. Danabasoglu, 2016: Atmospheric Conditions Associated with Labrador Sea Deep Convection: New Insights from a Case Study of the 2006/07 and 2007/08 Winters. *Journal of Climate*, **29 (14)**, 5281–5297, doi:10.1175/JCLI-D-15-0527.1.

Kolstad, E. W., T. J. Bracegirdle, and M. Zahn, 2016: Re-examining the roles of surface heat flux and latent heat release in a "hurricane-like" polar low over the barents sea. *Journal of Geophysical Research*, **121 (13)**, 7853–7867, doi: 10.1002/2015JD024633.

Markina, M. Y., and A. V. Gavrikov, 2016: Wave climate variability in the North Atlantic in recent decades in the winter period using numerical modeling. *Oceanology*, **56 (3)**, 320–325, doi: 10.1134/S0001437016030140.

Otte, T. L., C. G. Nolte, M. J. Otte, and J. H. Bowden, 2012: Does nudging squelch the extremes in regional climate modeling? *Journal of Climate*, **25 (20)**, 7046–7066, doi:10.1175/JCLI-D-12-00048.1.

Schneider, T., C. M. Kaul, and K. G. Pressel, 2019: Possible climate transitions from breakup of stratocumulus decks under greenhouse warming. *Nature Geoscience*, **12 (3)**, 164–168, doi: 10.1038/s41561-019-0310-1.

Skamarock, W. C., J. B. Klemp, J. Dudhia, D. O. Gill, and D. M. Barker, 2008: *A description of the Advanced Research WRF Version 3. NCAR Technical Note*. NCAR, Boulder, Colorado, 125 pp.

Tang, J., S. Wang, X. Niu, P. Hui, P. Zong, and X. Wang, 2017: Impact of spectral nudging on regional climate simulation over CORDEX East Asia using WRF. *Climate Dynamics*, **48 (7-8)**, 2339–2357, doi:10.1007/s00382-016-3208-2.

Relationship between shortwave radiation bias over the Southern Ocean and the ITCZ in MRI-ESM2

Hideaki Kawai (h-kawai@mri-jma.go.jp), **Tsuyoshi Koshiro, and Seiji Yukimoto**
Meteorological Research Institute, JMA

1. Introduction

Kang et al. (2008, 2009) showed that the ITCZ responds to heating in the extratropics using a slab-ocean model and explained the mechanism in terms of the energy budget. Hwang and Frierson (2013) found relationships between the radiation bias over the Southern Ocean and the ITCZ in CMIP5 multi-models. Kay et al. (2016) and Hawcroft et al. (2017) used atmosphere–ocean coupled models to show that the excess energy in the Southern Ocean is transported to the Northern Hemisphere more by the ocean than by the atmosphere.

The previous version of the MRI climate model, MRI-CGCM3, which was used for CMIP5 simulations, had a serious negative bias in the reflection of shortwave radiation due to an unrealistically small cloud radiative effect (CRE) over the Southern Ocean. The negative bias was reduced significantly in MRI-ESM2 (Yukimoto et al. 2019), which is used in the CMIP6 simulations. The improvement is achieved by the accumulation of modifications in various physical schemes related to clouds (Kawai et al. 2019). Therefore, we can intentionally increase the shortwave radiation bias over the Southern Ocean by turning the modifications back to the old treatments one by one. By doing this, we can quantitatively examine the relationship between shortwave radiation bias over the Southern Ocean and the ITCZ in MRI-ESM2.

2. Experiments

The control run (CNTL) uses the standard version of MRI-ESM2 and has the smallest shortwave radiation bias over the Southern Ocean. In the simulation EXP1, the new stratocumulus scheme (Kawai et al. 2017, 2019) that can better reproduce stratocumulus is replaced by the old scheme (Kawai and Inoue 2006). In MRI-ESM2, the occurrence of shallow convection is prevented over the area where the conditions for stratocumulus occurrence are met. This has the effect of increasing marine stratocumulus. EXP2 is as EXP1, but the shallow convection conditional prevention is turned off. EXP3 is as EXP2, but the treatment of the Wegener–Bergeron–Findeisen process is turned from the new one that increases the ratio of supercooled liquid clouds to the old one. In MRI-ESM2, the number concentration of cloud condensation nuclei originating from fine mode sea salt is doubled to take into account the marine aerosols in the Aitken mode that cannot be explicitly represented in the model. EXP4 is as EXP3 but with the doubling (described above) that results in an increase in the optical depth of marine low clouds turned off. See Kawai et al. (2019) for more details related to these processes. These experiments are listed in Table 1 and the radiation bias is expected to monotonically increase from CNTL to EXP4. We ran the historical simulations with these five settings using the atmosphere–ocean coupled model. The models were run from 2000 to 2014, and data for the ten years from 2005 to 2014 were used for analysis.

3. Results

The left panel in Fig. 1 shows that the shortwave radiation flux at the top of the atmosphere (TOA) over the Southern Ocean increases monotonically (downward: positive) from CNTL to EXP4. The middle panel in Fig. 1 shows that the net (shortwave + longwave) radiation flux at the TOA also increases monotonically

	CNTL	EXP1	EXP2	EXP3	EXP4
stratocumulus scheme	new	old	old	old	old
shallow convection conditional turning off	yes	yes	no	no	no
WBF effect	new	new	new	old	old
fine sea aerosols	yes	yes	yes	yes	no

Table 1: List of settings for experiments.

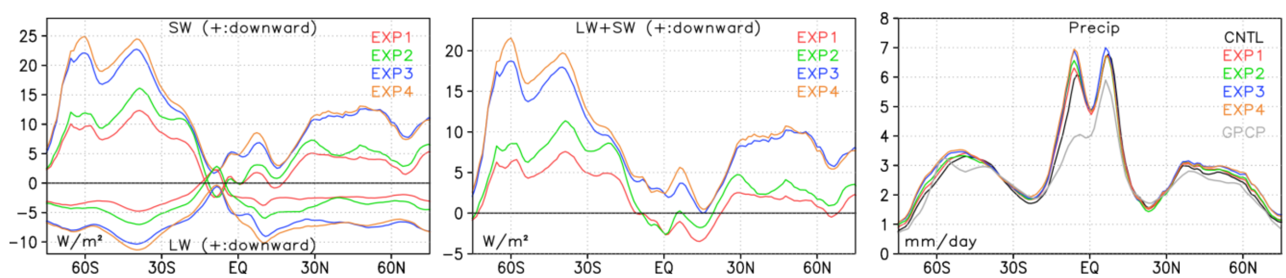

Fig. 1: Differences of shortwave and longwave radiative flux (left) and net (shortwave + longwave) radiative flux (middle) at TOA with respect to the control experiment for each experiment (unit: W/m^2, positive: downward). Precipitation (unit: mm/day) (right). Zonal means are plotted. MRI-ESM2 is used and the climatologies cover the period 2005–2014. GPCP observation period is 1979–2013.

from CNTL to EXP4, although the impact on shortwave radiation is partly compensated by the impact on longwave radiation. Actually, the impact on longwave radiation is caused more by the SST increase (i.e. clear sky radiation; ~70%) than changes in clouds (i.e. CRE; ~30%) (figure not shown). The right panel in Fig. 1 shows the impact on zonal mean precipitation. The peak in precipitation in the Southern tropics increases from CNTL to EXP4.

We calculated the asymmetry of extratropical radiative flux and CRE (Hwang and Frierson 2013), the tropical precipitation asymmetry index (Hwang and Frierson 2013), and the Southern ITCZ Index (Bellucci et al. 2010). Figure 2 shows clear relationships between the asymmetry of extratropical net radiative flux or CRE and tropical precipitation asymmetry or the Southern ITCZ Index. More extratropical radiative flux over the Southern Hemisphere than over the Northern Hemisphere corresponds to more tropical precipitation in the Southern Hemisphere than in the Northern Hemisphere or more precipitation over the Eastern Tropical Pacific in the Southern Hemisphere. Although the net (shortwave + longwave) radiation is used for the plots, the relationships essentially depend on the contribution of the shortwave component (figure not shown).

Figure 3 shows the impacts on energy transport relative to the control simulation. The impacts on the cross-equatorial northward energy transport are positive and the energy transport monotonically increases from CNTL to EXP4. The contribution of the ocean to the northward energy transport is almost twice the contribution of the atmosphere.

Although the change in transport by the ocean is larger than that by the atmosphere, as previous studies have shown, a clear relationship between the Southern Ocean radiation bias and ITCZ, as found by Hwang and Frierson (2013), is still seen in our simulations. It is possible that the alleviation of the double ITCZ problem in MRI-ESM2 compared to MRI-CGCM3 is partly attributable to the reduction of the Southern Ocean radiation bias.

Acknowledgements

This work was partly supported by the Integrated Research Program for Advancing Climate Models (TOUGOU) Grant Number JPMXD0717935561 from the Ministry of Education, Culture, Sports, Science and Technology (MEXT), Japan. It was also supported by the Japan Society for the Promotion of Science (JSPS) KAKENHI (Grant Nos. JP18H03363, JP19K03977, and JP19H05699), and the Environmental Restoration and Conservation Agency, Japan (the Environment Research and Technology Development Fund (Grant No. 2-2003)).

References

Bellucci, A., S. Gualdi, and A. Navarra, 2010: *J. Clim.*, **23**, 1127–1145.

Hawcroft, M., et al., 2017: *Clim. Dyn.*, **48**, 2279–2295.

Hwang, Y.-T., and D. M. W. Frierson, 2013: *Proc. Natl. Acad. Sci.*, **110**, 4935–4940.

Kang, S. M., et al., 2008: *J. Clim.*, **21**, 3521–3532.

Kang, S. M., D. M. W. Frierson, and I. M. Held, 2009: *J. Atmos. Sci.*, **66**, 2812–2827.

Kawai, H., and T. Inoue, 2006: *SOLA*, **2**, 17-20.

Kawai, H., T. Koshiro, and M. J. Webb, 2017: *J. Climate*, **30**, 9119-9131.

Kawai, H., et al., 2019: *Geosci. Model Dev.*, **12**, 2875–2897.

Kay, J. E., et al., 2016: *J. Clim.*, **29**, 4617–4636.

Yukimoto, S., et al., 2019: *J. Meteor. Soc. Japan*, **97**, 931–965.

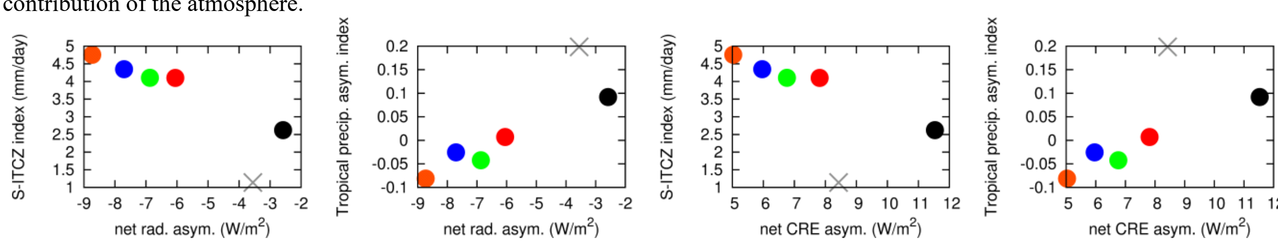

Fig. 2: Relationships between the asymmetry of extratropical net radiative flux or CRE and tropical precipitation asymmetry or the Southern ITCZ Index. The asymmetry of extratropical radiative flux or CRE is calculated as the average over 20°N–90°N minus that over 20°S–90°S (positive: downward, Hwang and Frierson 2013). The tropical precipitation asymmetry index is defined as the precipitation over 0°N–20°N minus that over 0°S–20°S normalized by the total tropical precipitation (20°S–20°N) (Hwang and Frierson 2013). The Southern ITCZ Index (mm/day) is defined as the annual mean precipitation over the 20°S–0°S, 100°W–150°W window (Bellucci et al. 2010). Crosses denote observations: CERES (2001–2010) for radiative flux and CRE, and GPCP (1979–2013) for precipitation. These plots use the same data as Fig. 1 and the colors of the symbols are shown in the panels in Fig. 1.

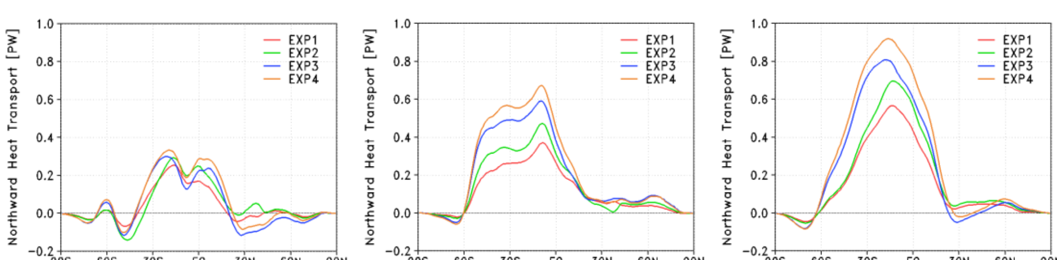

Fig. 3: Differences of northward heat transport by the atmosphere (left), the ocean (middle), and the sum (right) with respect to the control experiment (unit: PW). These plots use the same data as Fig. 1.

Does Radiative Cooling of Stratocumulus Strengthen Summertime Subtropical Highs?

Hideaki Kawai[1] (h-kawai@mri-jma.go.jp) **and Tsuyoshi Koshiro**[1]
[1]*Meteorological Research Institute, JMA*

1. Introduction

Some previous studies, including Liu et al. (2004), Wang et al. (2005), and Miyasaka and Nakamura (2005), have suggested that radiative cooling of stratocumulus (including stratus) might contribute to strengthening and/or localizing summertime subtropical highs. Our climate model MRI-ESM2 (Yukimoto et al. 2019), which is used in CMIP6 simulations, can represent low-level clouds such as subtropical stratocumulus relatively well and has a better score for radiative fluxes at the top of the atmosphere than any CMIP5 model (Kawai et al. 2019). In addition, stratocumulus off the west coast of continents can be completely removed in a physically consistent manner when the stratocumulus scheme is turned off in the model. Therefore, we can quantitatively examine the effect of radiative cooling of stratocumulus on subtropical highs by removing the clouds using a state-of-the-art global climate model that reproduces subtropical stratocumulus quite realistically.

2. Experiments

The model incorporates two stratocumulus schemes: the old one (Kawai and Inoue 2006) and the new one (Kawai et al. 2017, 2019). We ran the model with three settings: without a stratocumulus scheme, with the old scheme, and with the new scheme. We ran the model using two configurations: the atmospheric model (AMIP simulation) and the atmosphere–ocean coupled model (historical simulation). The models were run from 2000 to 2014, and data for the 10 years from 2005 to 2014 were used for analysis.

3. Results

3.1. Atmospheric model simulations

First, results from atmospheric model simulations for July are shown. As seen in Fig. 1, stratocumulus off the west coast of the continents, including off California, Peru, Mauritania, and Namibia, completely disappears when the stratocumulus scheme is turned off. When the old stratocumulus scheme is used, such clouds are represented more realistically. When the new stratocumulus scheme is used, all low-level clouds, including subtropical stratocumulus, are very similar to those observed. Although the negative bias in upward shortwave radiative flux at the top of the atmosphere due to the lack of reflection of solar radiation by stratocumulus is significantly large for the

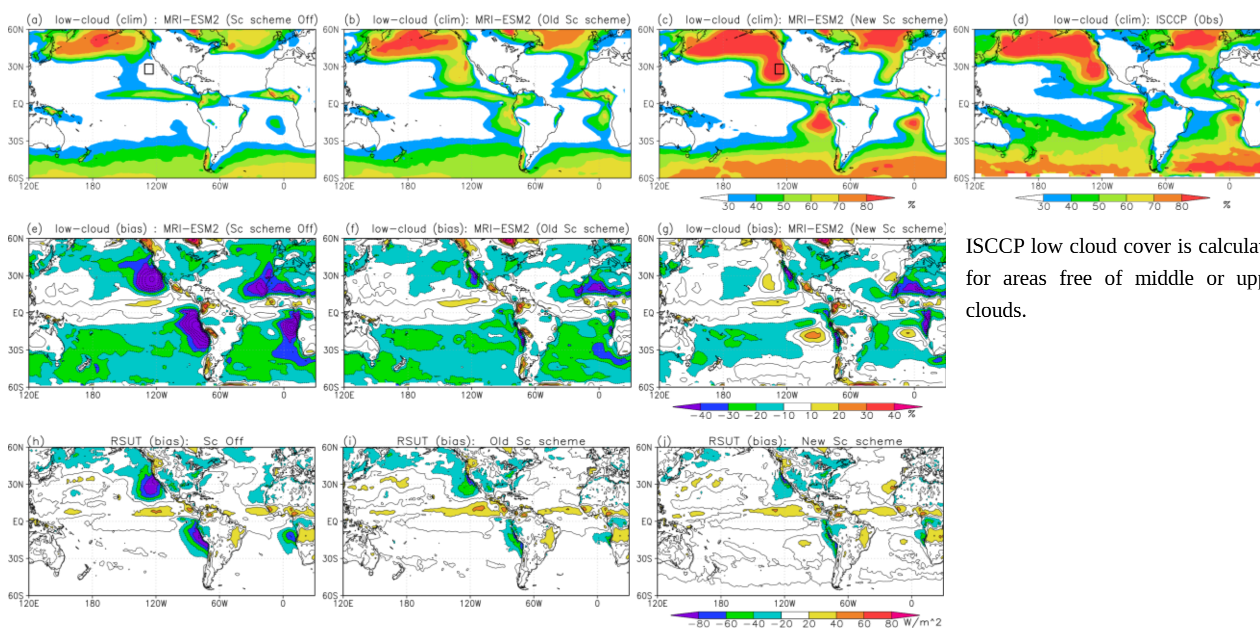

ISCCP low cloud cover is calculated for areas free of middle or upper clouds.

Fig. 1: From the top, climatologies of low cloud cover (%), biases of low cloud cover (%) with respect to ISCCP observations (shown in panel (d)), and biases of upward shortwave radiative flux (W/m^2) at the top of the atmosphere with respect to CERES-EBAF for July. From the left, results without stratocumulus schemes, with the old scheme, and with the new scheme. The climatologies cover the period 2005–2014 for model simulations and 1986–2005 for ISCCP data, and 2001–2010 for CERES-EBAF data.

simulation without a stratocumulus scheme, the bias is reduced for the simulation with the old stratocumulus scheme and is quite small for the new scheme simulation.

Figure 2 shows the impacts of the removal of stratocumulus on summertime subtropical highs as given by the difference between simulations with no stratocumulus scheme and with the old and new stratocumulus schemes. The figure shows that there is no change in the strength or locations of subtropical highs over the North Pacific and North Atlantic. Figure 3 shows the heating rate profiles of each physical process for the area off California shown by the box in Fig. 1a and 1c. It is clear that longwave cloud top cooling (about −14 K/day at the peak) is large when there are low clouds. However, most of the cooling is compensated by turbulent heating (5 K/day), heating by cloud condensation (6 K/day), and shortwave radiative heating (2 K/day). The response of the dynamics is relatively small. Therefore, cloud top cooling of stratocumulus cannot substantially change the strength of subtropical highs. This result is consistent with the fact that the strength of summertime subtropical highs was generally well represented in the JMA operational global model GSM even before 2004, although subtropical stratocumulus was not represented at all at the time (Kawai and Inoue 2006).

3.2. Coupled model simulations

The atmosphere–ocean coupled model simulations show results generally similar to those of the atmospheric model simulations. However, in the coupled model cases, subtropical highs can be altered through SST changes caused by the difference in solar insolation at the sea surface. Although SST is higher by 1–2 K in the simulation without a stratocumulus scheme owing to a lack of shielding of solar insolation, the decrease in pressure of the highs is only 1–2 hPa at the center of the highs (Figures not shown). A part of this decrease may even be attributed to the effect of SST increase over the global ocean, in addition to the effect of the local SST increase. Global SST increases over several years of model integration when the stratocumulus scheme is turned off, and it is known that subtropical highs are weaker for higher-SST conditions (e.g., Shaw and Voigt 2015, Kawai et al. 2018). The simulation results presented here lead us to conclude that no significant influence of radiative cooling of stratocumulus on summertime subtropical highs is identified in our simulations using a state-of-the-art climate model.

Acknowledgements

This work was partly supported by the Integrated Research Program for Advancing Climate Models (TOUGOU) Grant Number JPMXD0717935561 from the Ministry of Education, Culture, Sports, Science and Technology (MEXT), Japan. It was also supported by the Japan Society for the Promotion of Science (JSPS) KAKENHI Grant Numbers JP18H03363, JP19K03977, and JP19H05699.

References

Kawai, H., and T. Inoue, 2006: A simple parameterization scheme for subtropical marine stratocumulus. *SOLA*, **2**, 17–20.

Kawai, H., T. Koshiro, and M. J. Webb, 2017: Interpretation of Factors Controlling Low Cloud Cover and Low Cloud Feedback Using a Unified Predictive Index. *J. Climate*, **30**, 9119–9131.

Kawai, H., et al., 2018: Changes in Marine Fog over the North Pacific under Different Climates in CMIP5 Multi-Model Simulations. *J. Geophys. Res.*, **123**, 10,911–10,924.

Kawai, H., et al., 2019: Significant improvement of cloud representation in the global climate model MRI-ESM2. *Geosci. Model Dev.*, **12**, 2875–2897.

Liu, Y., et al., 2004: Relationship between the subtropical anticyclone and diabatic heating. *J. Clim.*, **17**, 682–698.

Miyasaka, T., and H. Nakamura, 2005: Structure and formation mechanisms of the northern hemisphere summertime subtropical highs. *J. Clim.*, **18**, 5046–5065.

Shaw, T. A., and A. Voigt, 2015: Tug of war on summertime circulation between radiative forcing and sea surface warming. *Nat. Geosci.*, **8**, 560–566.

Wang, Y., et al., 2005: Large-scale atmospheric forcing by southeast Pacific boundary layer clouds: A regional model study. *J. Clim.*, **18**, 934–951.

Yukimoto, S., et al., 2019: The Meteorological Research Institute Earth System Model version 2.0, MRI-ESM2.0: Description and basic evaluation of the physical component. *J. Meteor. Soc. Japan*, **97**, 931–965.

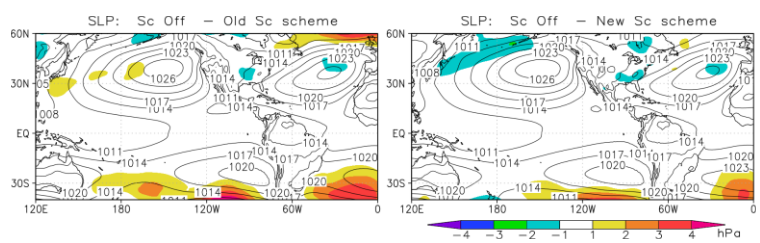

Fig. 2: Differences in climatologies of sea-level pressure for July for the period 2005–2014. Results without a stratocumulus scheme minus those (left) with the old scheme and (right) with the new scheme.

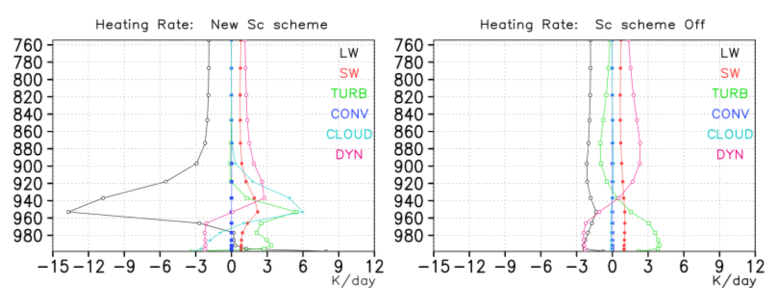

Fig. 3: Heating-rate profiles for each physical process for the area off California shown in Fig. 1a and 1c for July. Heating rate for longwave (black) and shortwave (red) radiation, turbulence (green), convection (blue), cloud (light blue), and dynamic (pink) processes with the new stratocumulus scheme (left) and without a scheme (right) for the period 2005–2014 are shown. The vertical axis shows pressure (hPa).

Impact of Cloud Microphysics Parameter on 20th Century Warming Simulated in MRI-CGCM3

Tsuyoshi Koshiro, Hideaki Kawai, and Seiji Yukimoto

Meteorological Research Institute, Tsukuba, Japan

e-mail: tkoshiro@mri-jma.go.jp

1 Introduction

Recently, the treatment of clouds in global climate models has become more sophisticated. However, physics schemes related to clouds have a number of adjustable parameters; they are tuned to achieve the desired radiation balance for the best representation of the observed climate. Golaz et al. (2013) showed that variations in the autoconversion threshold radius (r_{crit}), which controls the conversion of cloud water to rain, result in significantly different temperature evolutions over the 20th century in the CMIP5 GFDL-CM3 model. They suggested the presence of compensating model errors; the model characterized by the most plausible value of r_{crit} ($\sim$ 10 µm, derived from satellite observations; e.g., Suzuki et al., 2013) produced very unrealistic 20th century temperature evolutions.

In this study, we perform experiments similar to the aforementioned study to demonstrate the impact of the cloud microphysics parameter r_{crit} on the 20th century warming simulated by the CMIP5 MRI-CGCM3 model (Yukimoto et al., 2012). Golaz et al. (2013) regulated two additional parameters associated with cloud processes to keep the radiation balance within a desirable range; however, we vary only the value of r_{crit} to examine the climate response purely to this parameter. Moreover, we investigate the simulated cloud properties that may have caused the different temperature evolutions over the 20th century.

2 Method

We conducted two sets of CMIP5 MRI-CGCM3 historical simulations with alternative configurations of the r_{crit} value. We selected r_{crit} values smaller (5.0 µm, MRI-CGCM3w) and larger (10.0 µm, MRI-CGCM3c) than the default value used in MRI-CGCM3 (7.0 µm). The AMIP experiments (i.e., atmosphere-only experiments forced with observed sea surface temperatures) with these configurations confirmed that the top-of-atmosphere (TOA) net radiation values were within the acceptable range for the comparison of this study (Table 1). Initially, we performed preindustrial spin-up integrations for MRI-CGCM3w and MRI-CGCM3c, branching from the initial condition of the CMIP5 MRI-CGCM3 preindustrial control (piControl) simulation. These spin-up integrations were run for 100 years, so that the climate system could adjust to the modified r_{crit} over shorter time scales. The piControl simulations started from the final spin-up states. Subsequently, we created an ensemble of three historical members (1851–2005) starting every 30 years from the piControl simulations. Each piControl simulation was run for 215 years to cover the whole period of the historical ensemble.

Table 1: Summary of model configurations (r_{crit} values) with TOA net downward radiation for 1979–2008 obtained from the AMIP experiments.

	r_{crit} (µm)	TOA rad. (W m^{-2})
MRI-CGCM3w	5.0	−0.28
MRI-CGCM3 (CMIP5)	7.0	−1.04
MRI-CGCM3c	10.0	−3.52

3 Results

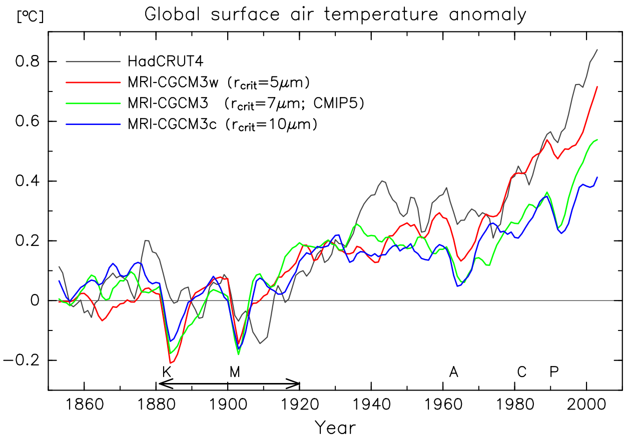

Fig. 1: Historical time series of global mean surface air temperature anomalies. Colored lines represent the CMIP5 MRI-CGCM3 model (green) and the two alternative configurations, MRI-CGCM3w (red) and MRI-CGCM3c (blue). Each line is a three-member ensemble average. Anomalies are calculated with respect to the period 1881–1920. Model drift is removed by subtracting the linear trend of the corresponding period in the piControl simulation from each ensemble member. Observations from HadCRUT4 (Morice et al., 2012) are also shown. A five-year running mean is applied to model results and observations. Letters above the horizontal axis represent major volcanic eruptions: Krakatoa (K), Santa María (M), Agung (A), El Chichón (C), and Pinatubo (P).

Figure 1 shows the temporal evolution of the global mean surface air temperature anomalies based on the CMIP5 MRI-CGCM3 historical simulations which considered different r_{crit} values. The standard CMIP5 MRI-CGCM3 underestimates the warming observed during the second half of the 20th century. MRI-CGCM3w more closely reflects the observations, except for the observed downward trend between the 1940s and 1970s. MRI-CGCM3c is generally colder than MRI-CGCM3, with indiscernible warming during the last period of the simulation. While the temperature from the HadCRUT4 observations increases by 0.59°C between 1881–1920 (preindustrial; denoted as PI) and 1981–2005 (present day; denoted as PD), the results of MRI-CGCM3w, MRI-CGCM3, and MRI-CGCM3c indicate temperature increases of 0.52°C, 0.36°C, and 0.31°C, respectively, for the same period. These results are consistent with Golaz et al. (2013), although the differences in the temperature evolutions among the configurations are smaller than their results.

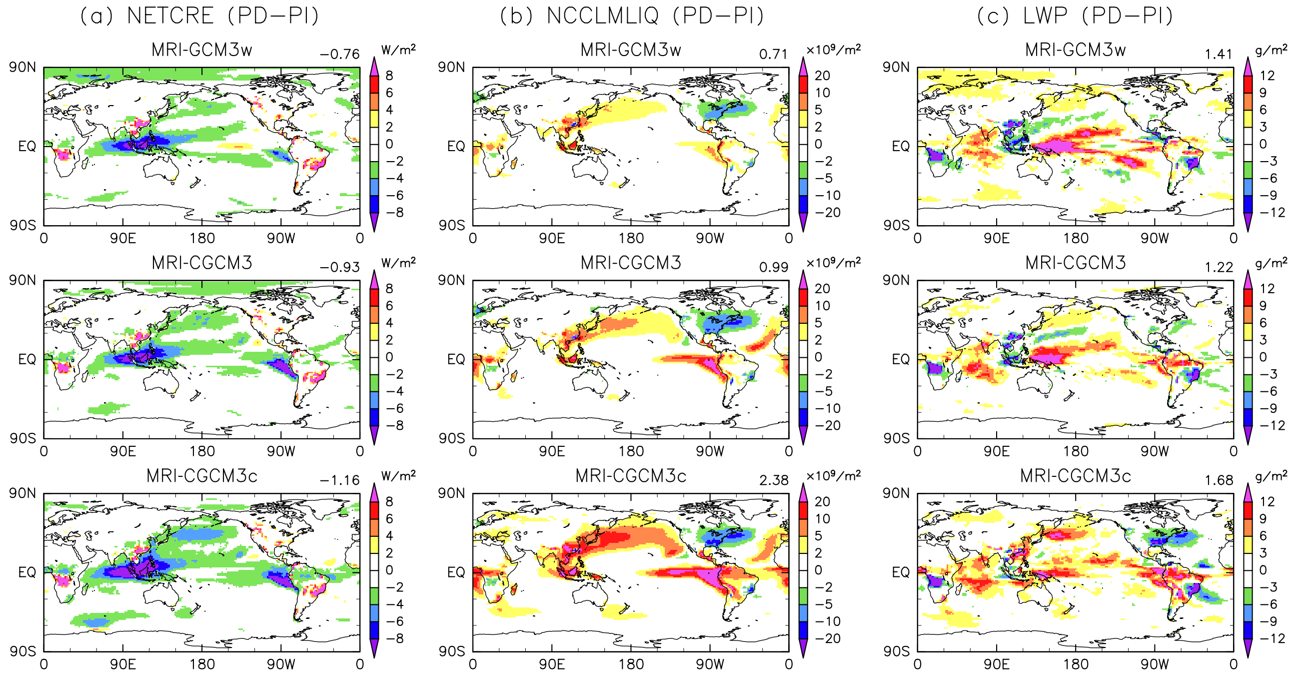

Fig. 2: PD–PI differences in annual and three-ensemble means of (a) net CRE (W m^{-2}; positive downwards), (b) column CDNC (10^9 m^{-2}), and (c) LWP (g m^{-2}) for MRI-CGCM3w (top), MRI-CGCM3 (middle), and MRI-CGCM3c (bottom). Global mean values are indicated at the top right of each panel.

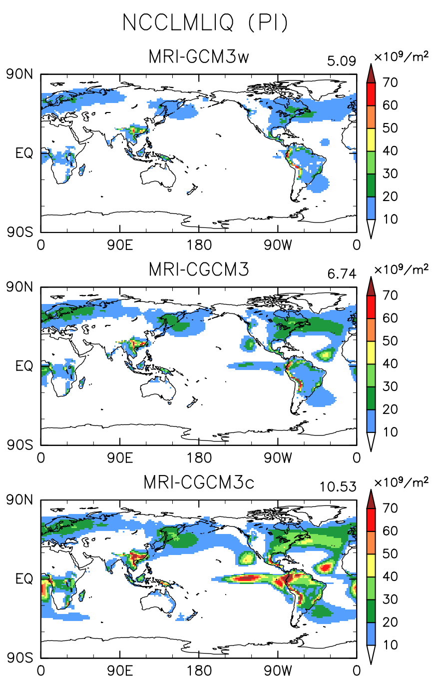

Fig. 3: Similar to Fig. 2b, but for PI annual and three-ensemble means.

Figure 2 displays the PD–PI differences in cloud properties for the three sets of the historical simulations. Figure 2a indicates that the differences between 20th century temperature evolutions are due to the net cloud radiative effect (CRE); the stronger the cloud radiative cooling (caused by shortwave solar reflection; not shown), the more underestimated the 20th century warming. The global mean values of the PD–PI difference in the net CRE are −0.76 W m^{-2}, −0.93 W m^{-2}, and −1.16 W m^{-2} in the case of MRI-CGCM3w, MRI-CGCM3, and MRI-CGCM3c, respectively. The absolute values of the negative net CRE and their variations among the configurations are large in the tropical eastern Pacific, the midlatitude North Pacific, and the western Maritime Continent.

As shown in Fig. 2b, these maxima are related to the column cloud droplet number concentration (CDNC). Notably, the differences in column CDNC among the configurations are largely derived from the baseline values of column CDNC under PI condition (Fig. 3); these differences grow further under PD conditions, due to the indirect effect of anthropogenic aerosols. The negative net CRE maxima over the subtropical North Pacific are more closely related to the liquid water path (LWP) than to the column CDNC; however, their differences among the configurations are not systematically clear (Fig. 2c). The baseline values of LWP (not shown) are comparable for different configurations.

Considering the baseline values shown in Fig. 3, our results are in contrast to the simple expectation that an increase in r_{crit} would lead to an increase in LWP, but would not significantly affect the CDNC. Further analysis is required to understand the behavior of cloud-to-rain conversion processes in MRI-CGCM3 for different r_{crit} values.

Acknowledgments

This work was supported in part by the Integrated Research Program for Advancing Climate Models (TOUGOU) Grant Number JPMXD0717935561 from the Japanese Ministry of Education, Culture, Sports, Science and Technology (MEXT), the Japan Aerospace Exploration Agency (JAXA) 2nd Research Announcement on the Earth Observations, the Environment Research and Technology Development Fund (2-2003) of the Environmental Restoration and Conservation Agency (ERCA) of Japan, and the Japan Society for the Promotion of Science (JSPS) KAKENHI Grant Numbers JP18H03363, JP19K03977.

References

Golaz, J.-C., L. W. Horowitz, and H. Levy II, 2013: Cloud tuning in a coupled climate model: Impact on 20th century warming. *Geophys. Res. Lett.*, **40**, 2246–2251, doi:10.1002/grl.50232.

Morice, C. P., and Coauthors, 2012: Quantifying uncertainties in global and regional temperature change using an ensemble of observational estimates: The HadCRUT4 data set. *J. Geophys. Res.*, **117**, D08101, doi:10.1029/2011JD017187.

Suzuki, K., J.-C. Golaz, and G. L. Stephens, 2013: Evaluating cloud tuning in a climate model with satellite observations. *Geophys. Res. Lett.*, **40**, 4464–4468, doi:10.1002/grl.50874.

Yukimoto, S., and Coauthors, 2012: A new global climate model of the Meteorological Research Institute: MRI-CGCM3 —Model description and basic performance—. *J. Meteor. Soc. Japan*, **90A**, 23–64, doi:10.2151/jmsj.2012-A02.

Future projection of Indian summer monsoon variability under climate change scenario: Results from CMIP5/CCSM4 model simulation

Sujata K. Mandke[1,*] and Amita Prabhu[1]
[1]Indian Institute of Tropical Meteorology, Ministry of Earth Sciences, INDIA
*amin@tropmet.res.in, amitaprabhu@tropmet.res.in

1. Introduction

Considering the inherent complexities in the monsoon system and its strong sensitivity to global warming (Kitoh et al., 2013), simulations and projections of monsoon variability (Turner, 2011) have remained a challenge to the climate research community. Numerous modeling studies over last two decades have provided quantitative estimates of the monsoon variability in future (Wang et al., 2020). Nevertheless, the possible modulation of the inter-annual variability (IAV) of Indian summer monsoon rainfall (ISMR) by climate change still remains largely uncertain (IPCC, 2007). In this study, we address this issue by analyzing the simulations for the current and future projections of IAV of ISMR, using 20th century historical and 21st century projections with three Representative Concentration Pathways (RCP) scenarios by CCSM4 model from fifth Coupled Model Intercomparison Project (CMIP5; Taylor et al., 2012). CCSM4 model is selected due to its high horizontal resolution and modest ISMR climatology with respect to the observation (Prabhu and Mandke, 2019).

2. Data

Monthly mean precipitation (mm/day) data of CCSM4 model for the reference period (1861-2005; RP) of the 20^{th} century historical and three RCP scenarios (2.6, 4.5 and 8.5), for the period (2006-2100) of the 21^{st} century from CMIP5 (http://www-pcmdi.llnl.gov), are used.

3. Results

The IAV (bars), trend in IAV (dashed line) and decadal variability (shading) of summer monsoon precipitation averaged over India (8^0N-38^0N; 68^0E-98^0E) in historical and three RCP simulations of CCSM4 model from CMIP5 are depicted in figures 1a, 1b, 1c, and 1d respectively. A decrease in amplitude of both IAV and decadal variability in all three RCPs with respect to RP is noticed. There is consensus in IAV and decadal variability among three RCPs. The trend in the IAV is insignificant in both historical and three RCPs. The limitation of this study is the analysis of single model, which will be substantiated in future with multi-models.

References

IPCC, 2007: Climate change 2007 – The physical science basis contribution of working group I to the fourth assessment report of the IPCC (ISBN 978 0521 88009-I Hardback; 0521 70596-7.

Kitoh, A., Endo, H., Krishna Kumar, K. and coauthors, 2013: Monsoons in a changing world: A regional perspective in a global context. J. Geophys. Res. Atmos. 118, 3053–3065.

Prabhu, Amita and Mandke, Sujata, 2019: Indian rainfall and Eurasian snow climatology in CMIP5 historical simulations. Research activities in atmospheric and oceanic modeling, CAS/JSC Working Group on Numerical Experimentation. Report No. 49. WCRP Report No.12/2019. WMO, Geneva, pp. 9-03 - 9-04.

Taylor K.E., Stouffer R.J. and Meehl G.A., 2012: An overview of CMIP5 and the experiment design, Bull. Amer. Meteorol. Soc, 90,4 :85–498.

Turner, A.G., 2011: Modelling monsoons: Understanding and predicting current and future behaviour. In: Chang, C., Ding, Y., Lau, N., et al. (Eds.), Glob. Monsoon Syst. Res. Forecast, 2nd edition, World Scientific; WMO, 421–454.

Wang B. and 24 coauthors, 2020: Monsoons Climate change assessment. BAMS (Early online release) DOI 10.1175/BAMS-D-19-0335.1

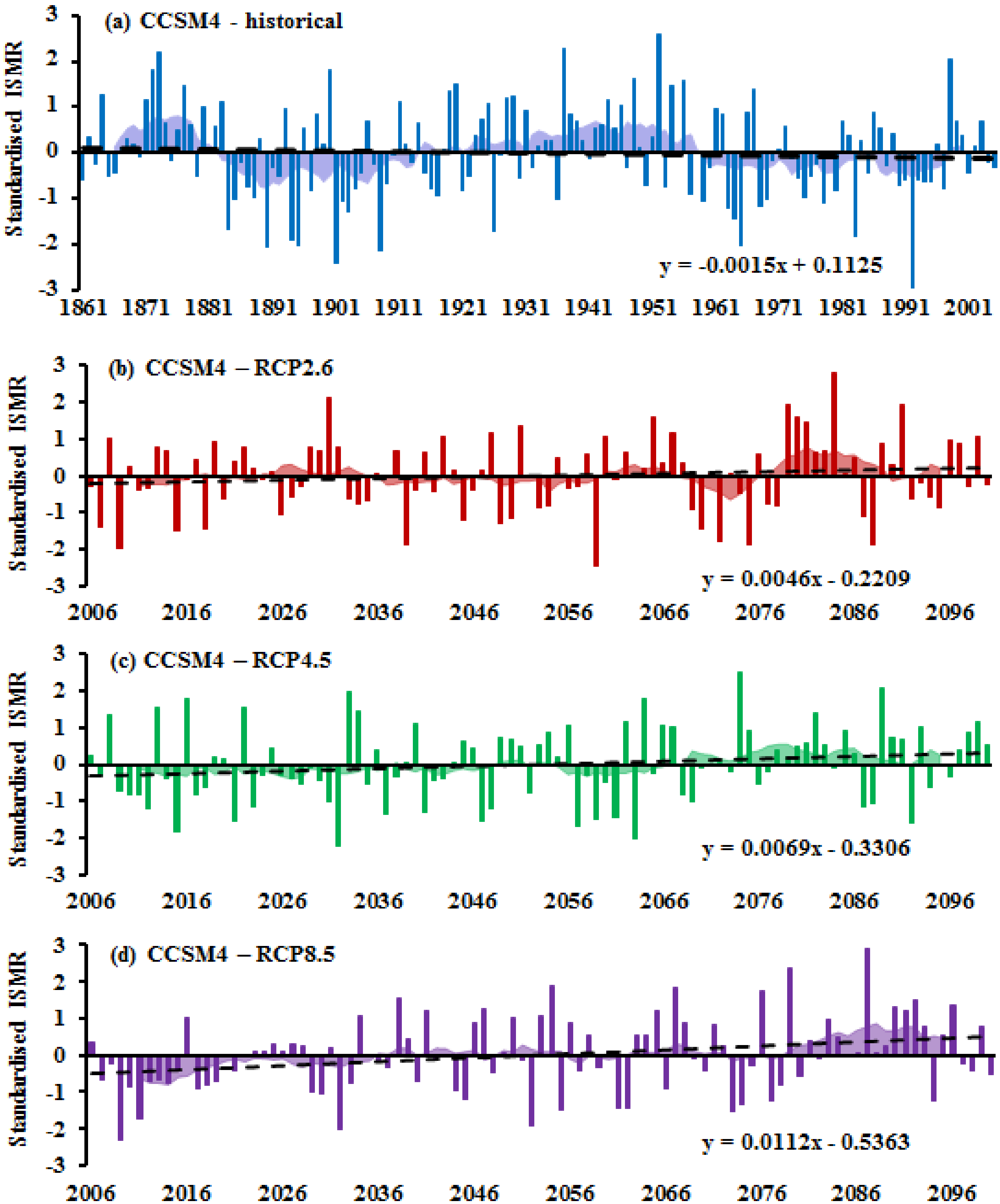

Figure 1: Inter-annual variability of precipitation over India simulated by CCSM4 model from CMIP5. Colored bars (year-to-year variations); Shading (decadal variability); Black dashed line (trend) (a) Historical run (b) RCP2.6 (c) RCP4.5 (d)RCP8.5

Atmospheric temperature stratification in dependence on the annual cycle length: Numerical experiments with climate model of general circulation

I.I. Mokhov[1,2] and A.V. Timazhev[1]

[1]A.M. Obukhov Institute of Atmospheric Physics RAS
[2]Lomonosov Moscow State University
mokhov@ifaran.ru, timazhev@ifaran.ru

Numerical simulations were carried out with the climate model of general circulation (CGCM) for different lengths of the annual cycle. The model results confirm the conclusion made from the analysis of temperature data with the use of special method of amplitude-phase characteristics [1,2]. According to the results obtained in [1,2], the height of the troposphere (tropopause) corresponds to the height of the temperature skin layer for the atmosphere periodically heated from the surface in the annual cycle [3]. In particular, according to model simulations, the tropopause height *H* for a shorter period *T* of the annual cycle was correspondingly lower.

We analyzed simulations with the CGCM version used in [4]. This CGCM version uses the general atmospheric circulation unit ECHAM5 [5] and the general ocean circulation unit MOM5 [6]. Atmospheric (T31L39) and oceanic (with a resolution of 1.125°x1.125°) blocks are combined using the OASIS communication system [7]. In our numerical experiments we used different lengths of the annual cycle for solar irradiance as an external periodic forcing for the climate system. In [4], in particular, the analysis of the results of control simulations for a 150-year period were carried out. Simulations with this GCM (hereinafter IAP RAS GCM) indicate an adequate reproduction of the main features of modern distributions for key climate characteristics (including surface air temperature, sea level pressure, precipitation etc.). Also, a quite adequate reproduction of the key features of the El Niño quasi-cyclic processes, with which the strongest interannual variability of the global surface temperature is associated, was noted. In particular, the model is able to reproduce the features of the repeatability of phase transitions for El Niño processes [4].

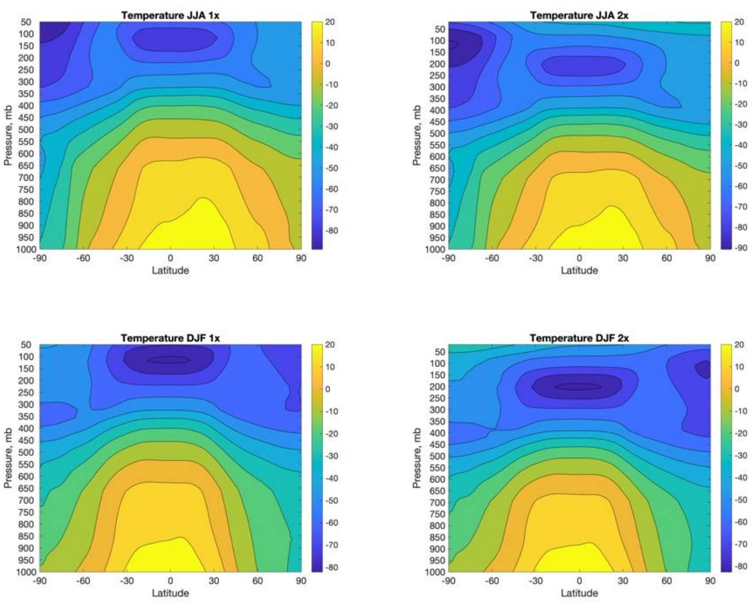

Fig. 1. Seasonal latitude-altitude temperature distributions in the atmosphere in June-July-August (upper row) and December-January-February (lower row) from model simulations with the current length T_o of the annual cycle (left) and with the length $T_o/2$ (right).

Figure 1 presents seasonal latitude-altitude temperature distributions in the atmosphere in June-July-August and December-January-February from model simulations with the current length T_o (365 days) of the annual cycle and with the $T_o/2$ period. According to Fig. 1, both in summer and winter, at twice the annual frequency, the height of the corresponding isotherms at all latitudes decreases. This is especially clearly manifested in a decrease in the region with minimal temperature in the vicinity of the tropical tropopause.

Figure 2 shows the vertical temperature profiles in the atmosphere of different latitudes in the summer from the IAP RAS GCM simulations for the T_o and $T_o/2$ periods of the annual cycle. Similar profiles were obtained for other latitudes of the Northern and Southern Hemispheres for the different seasons. According to Fig. 2, the values of the tropopause height, characterized by an abrupt change in the temperature profile, vary according to model simulations for the T_o length of the annual cycle from about 15 km near the equator to about 8 km in the polar regions. With the $T_o/2$ length of the annual cycle the tropopause height is about 11 km near the equator and about 6-7 km in the polar regions.

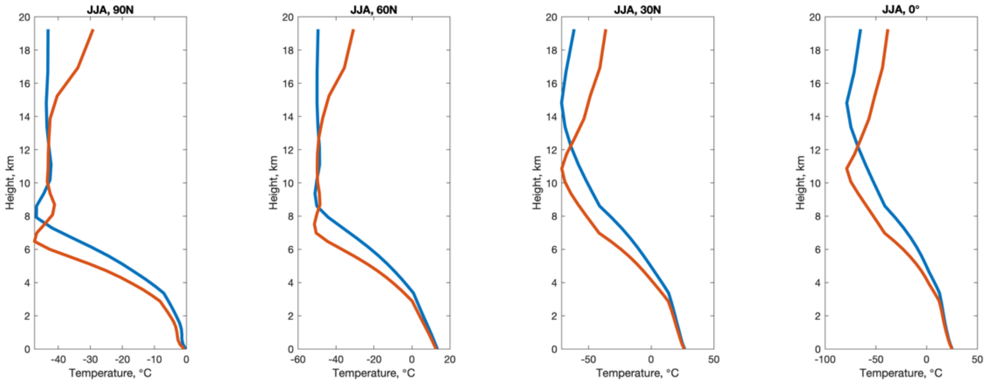

Fig. 2. Vertical temperature profiles in the atmosphere of different latitudes in the summer from model simulations for two lengths of the annual cycle: T_o (blue lines) and $T_o/2$ (red lines).

An analysis of H values at different latitudes from model simulations with the different annual cycle lengths T indicates that relationship between H and T corresponds to the root dependence $H \sim T^{1/2}$. It is similar to the appropriate dependence for the characteristic depth of the heat wave penetration associated with periodic forcing (skin-effect) as was suggested in [1,2].

The analysis was carried out in the framework of the RSF project 19-17-00240.

References

1. Mokhov I.I. (1985) Method of amplitude-phase characteristics for analyzing climate dynamics. *Sov. Meteorol. Hydrol.*, 5, 14-23.
2. Mokhov I.I. (1985) Analysis of annual course of climate characteristics. *Sov. Meteorol. Hydrol.*, 9, 31–37.
3. Mokhov I.I. (1993) Diagnostics of Climate System Structure. Gidrometeoizdat, St. Petersburg, 271 pp.
4. Mokhov I.I., Timazhev A.V. Summer climate anomalies in the Northern Eurasia during intra-annual transitions from El Niño to La Niña. *Research Activities in Atmospheric and Oceanic Modelling*. E. Astakhova (ed.). 2016. WCRP Rep. No.15/2016. S. 6. P. 7–8.
5. Roeckner E. et al. (2003) The Atmospheric General Circulation Model ECHAM5. Part I: Model Description. MPI Report 349, Max Planck Institute for Meteorology, Hamburg, Germany, 90 pp.
6. Griffies S.M. (2012) Elements of the Modular Ocean Model (MOM). NOAA/Geophysical Fluid Dynamics Laboratory. GFDL Ocean Group Techn., Rep. No. 7, 632 pp.
7. Valcke S. (2013) The OASIS3 coupler: a European climate modelling community software. *Geosci. Model Dev.*, **6**, 373-388.

Spatial features of snow over Eurasia and precipitation over India in the warming scenarios: CCSM4 model projections from CMIP5

Amita Prabhu[1] and Sujata K. Mandke[1,*]

[1]Indian Institute of Tropical Meteorology, Ministry of Earth Sciences, INDIA

amitaprabhu@tropmet.res.in, *amin@tropmet.res.in

Introduction

Multimodel projections indicate significant decrease in snow water equivalent for most of the regions of the Northern hemisphere (Shi and Wang, 2015) and an increase in the mean precipitation over South Asian summer monsoon region in greenhouse gases induced warmer climate during the 21st century relative to the present (Wang et al. 2020). However, there is little agreement between models in projections of snow (Collins et al. 2013) and regional precipitation throughout vast areas of the tropics (Rowell 2012). Linkage between Eurasian snow in the preceding season and Indian summer monsoon rainfall (ISMR) has been extensively documented (Kripalani and Kulkarni, 1999). Understanding how the spatial features of Eurasian snow and ISMR may change in the future remains a grand challenge. In this study, we provide insights into the spatial characteristics of projected changes in winter snow over Eurasia and summer monsoon precipitation (SMP) over India for the 21st century under three different Representative Concentration Pathways (RCP) scenarios of CCSM4 model from Coupled Model Intercomparison Project phase 5 (CMIP5; Taylor et al., 2012).

Data

Monthly mean precipitation and snowfall flux of CCSM4 model for the reference period (1975-2005; RP) of 20th century historical and three RCP scenarios namely RCP2.6, 4.5 8.5 from CMIP5 (http://www-pcmdi.llnl.gov) are used. The future change in three RCPs for the period 2020-2100 of 21st century is evaluated over two sub-periods separately: an early-to-middle (2020-2050; EMP) and late period (2070-2100; LP).

Results

Projected spatial changes in winter snowfall flux (WSF) over Eurasia during EMP relative to RP in CCSM4 model from CMIP5 are shown for RCPs 2.6, 4.5 and 8.5 in figures 1a, 1b, and 1c respectively. Similar projected spatial changes in SMP over India are shown in figures 1d, 1e and 1f respectively for three RCPs. Likewise, projected spatial changes in WSF over Eurasia and SMP over India are analyzed for three RCPs (figure 2 [a-e]) during LP. The model projects significant decreases in WSF during the EMP over region encompassing northwestern Eurasia extending southeastward to 90°E, in RCP 8.5, whereas decrease is confined to very small pockets from west to central Eurasia in RCPs 2.6 and 4.5. The only region with projected increase in WSF is north-central and north-eastern Eurasia in RCP2.6, which reduces in spatial extent from RCPs 4.5 to 8.5. Spatial features of projected WSF during LP (Fig 2(a-c)) are mostly analogous to EMP (Fig. 1(a-c)), but with larger spatial extent of reduction in WSF. Also, the magnitude and spatial spread of projected decrease in WSF during LP exhibit gradual increase from RCPs 2.6 to 8.5 (Figure 2(a-c)), as evident over whole of west and central Eurasia in RCP8.5 (Fig. 2c). Significant increase in WSF during LP over small portion of extreme northeastern Eurasia in RCP2.6 displays steady growth in its spatial expanse from RCPs 2.6 to 8.5 (Fig. 2(a-c)).

Significant increase in SMP during EMP relative to RP in CCSM4 model is projected over northeast, west and southeast peninsular India in RCP 2.6 (Fig. 1d), with further increase in its spatial spread from RCPs 2.6 to 8.5 (Fig. 1(d-f)). Projected spatial characteristics of SMP during LP (Fig 2(d-f)) are mostly analogous to that during EMP (Fig. 1(d-f)). Projected changes in WSF and SMP in CCSM4/CMIP5 model in the present study are in consensus with the earlier studies mentioned in introduction.

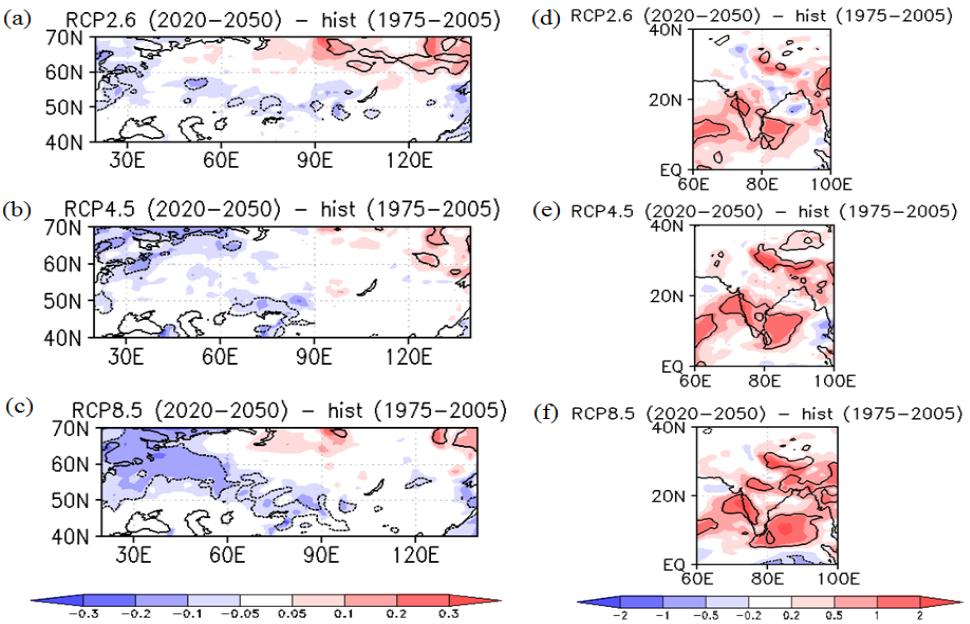

Fig. 1: Projected change in WSF (mm day^{-1}) over Eurasia (a-c) and SMP (mm day^{-1}) over India (d-f) for three RCPs by CCSM4 model from CMIP5 during EMP relative to RP. Black solid contour indicates statistical significance at 95% level.

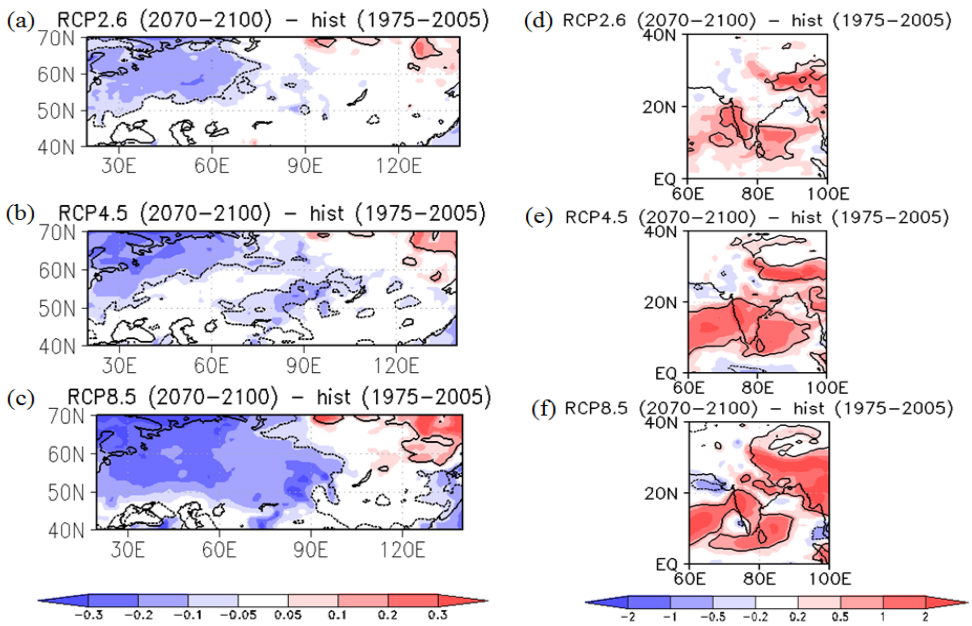

Fig. 2 (a-f): Same as in Figure 1 (a-f) except during LP relative to RP

References

Collins, M., and Coauthors, 2013: Long-term climate change: Projections, commitments and irreversibility. Climate Change 2013: The Physical Science Basis. T. F. Stocker et al., Eds., Cambridge University Press, 1029–1136,

Kripalani RH, Kulkarni A, 1999: Climatology and variability of historical Soviet snow depth data: some new perspectives in snow-Indian monsoon teleconnections. Climate Dynamics. 15:475–489

Rowell, D., 2012: Sources of uncertainty in future changes in local precipitation. Climate Dyn., 39, 1929–1950, doi:10.1007/ s00382-011-1210-2.

Shi, H. X., and C. H. Wang, 2015: Projected 21st century changes in snow water equivalent over Northern Hemisphere landmasses from the CMIP5 model ensemble. Cryosphere, 9, 1943–1953, doi:10.5194/tc-9-1943-2015

Taylor, K. E., Stouffer, R. J., and Meehl, G. A.2012: An Overview of CMIP5 and the experiment design, B. Am. Meteor Soc., 93,485–498

Wang B. and 24 coauthors, 2020: Monsoons Climate change assessment. BAMS (Early online release) DOI 10.1175/BAMS-D-19-0335.1